A Journal of the Gesellschaft Deutscher Chemiker

Angewandte International Edition GDCh Chemie

www.angewandte.org

Accepted Article

Title: Lewis Acid Strength of Interfacial Metal Sites Drives CH3OH Selectivity and Formation Rates on Cu-based CO2 Hydrogenation Catalysts

Authors: Christophe Copéret, Gina Noh, Erwin Lam, Daniel T. Bregante, Jordan Meyet, Petr Šot, and David W. Flaherty

To be cited as: *Angew. Chem. Int. Ed.* 10.1002/anie.202100672

Link to VoR: https://doi.org/10.1002/anie.202100672

WILEY-VCH

10.1002/anie.202100672

WILEY-VCH

RESEARCH ARTICLE

Lewis Acid Strength of Interfacial Metal Sites Drives CH_3OH Selectivity and Formation Rates on Cu-based CO_2 Hydrogenation Catalysts

Gina Noh,[a] Erwin Lam,[a] Daniel T. Bregante,[b] Jordan Meyet,[a] Petr Šot,[a] David W. Flaherty,[b] Christophe Copéret*[a]

[a] Dr. G. Noh, Dr. E. Lam, J. Meyet, Dr. P. Šot, Prof. Dr. C. Copéret
Department of Chemistry and Applied Biosciences
ETH Zürich
Vladimir Prelog Weg 1-5, 8093 Zürich (Switzerland)
E-mail: ccoperet@inorg.chem.ethz.ch

[b] Dr. D. T. Bregante, Prof. Dr. D. W. Flaherty
Department of Chemical and Biomolecular Engineering
University of Illinois at Urbana-Champaign
Urbana, IL 61801 (United States)

Supporting information for this article is given via a link at the end of the document.

Abstract: CH_3OH formation rates in CO_2 hydrogenation on Cu-based catalysts sensitively depend on the nature of the support and the presence of promoters. In this context, Cu nanoparticles supported on tailored supports (highly dispersed M on SiO_2; M = Ti, Zr, Hf, Nb, Ta) were prepared via Surface Organometallic Chemistry, and their catalytic performance was systematically investigated for CO_2 hydrogenation to CH_3OH. The presence of Lewis acid sites enhances CH_3OH formation rate, likely originating from stabilization of formate and methoxy surface intermediates at the periphery of Cu nanoparticles, as evidenced by metrics of Lewis acid strength and detection of surface intermediates. The stabilization of surface intermediates depends on the strength of Lewis acid M sites, described by pyridine adsorption enthalpies and ^{13}C chemical shifts of $-OCH_3$ coordinated to M; these chemical shifts are demonstrated here to be a molecular descriptor for Lewis acid strength and reactivity in CO_2 hydrogenation.

Introduction

CO_2 hydrogenation to CH_3OH is part of a virtuous closed-carbon cycle, together with H_2 production from intermittent excess renewable energy. Such a strategy mitigates anthropogenic CO_2 emissions while simultaneously generating a valuable molecule that is either directly compatible with existing petroleum infrastructure or can be further upgraded.[1,2] Cu-based catalysts are widely studied because of their low selectivity to over-reduced products (e.g., CH_4); however, their reactivity in CO_2 hydrogenation reactions and their selectivity to CH_3OH, rather than to CO, depend strongly on the nature and identity of the support and promoters.[3–6] Improving catalytic performance remains challenging, in part, because these support and promoter effects are not understood on a molecular level. For example, there have been conflicting evidence and requirements for reducible oxides that facilitate redox reactions[7–9] and for undercoordinated metal centers that act as Lewis acid sites[4,5,10,11] to facilitate CO_2 adsorption and/or stabilize reaction intermediates. In addition, unsupported Cu surfaces show lower performance than Cu supported on metal oxides,[12] indicating the importance of Cu-support interfaces.

Cu-support interfacial sites have been implicated in selective (de)hydrogenation[13,14] and hydrodeoxygenation[15] reactions, among others. Consequently, understanding and tuning properties of interfaces is crucial to developing more efficient heterogeneous catalysts, not only for CO_2 hydrogenation reactions but also for a broad array of reactions catalysed by supported metal nanoparticles.[16] In CO_2-to-CH_3OH hydrogenation reactions, interfacial sites—Zr(IV) or Ti(IV), dispersed on SiO_2 or present in ZrO_2 and TiO_2—at the periphery of Cu nanoparticles act as Lewis acid sites to stabilize surface formate and methoxide intermediates.[17–21] These sites thereby lead to increased CH_3OH formation rates and selectivities compared to Cu/SiO_2 (where the "Cu/X" nomenclature denotes Cu nanoparticles supported on X support). However, a clear relationship between Lewis acid strength of the interfacial sites and CH_3OH formation rates has not yet been established for these bifunctional systems.

We reasoned that using a Surface Organometallic Chemistry (SOMC) approach[22–25] would enable the preparation of Cu-based catalysts with varied promoters that had the same physicochemical properties (e.g., Cu dispersion, promoter loading). These materials would therefore be ideal candidates to investigate the relationship between the Lewis acid strength of interfacial sites and CH_3OH formation rates, in order to provide guidelines for rationally designing catalysts.

Here, we use a SOMC approach to synthesize Cu nanoparticles supported on SiO_2 decorated with selected dispersed early transition-metal Lewis acid sites, namely Ti, Zr, Hf, Nb, and Ta because of their differences in electronegativity and expected acid strength.[26,27] Infrared (IR) spectroscopy, N_2O titrations, transmission electron microscopy (TEM), mass balance analysis, and nuclear magnetic resonance (NMR) spectroscopy demonstrate that this synthetic approach provides materials that differ only in the Lewis acid strength of their early transition metal centers. These catalysts promote CH_3OH formation rates and selectivities in a manner related to the strength of their Lewis acid sites, which is assessed here using enthalpies of pyridine adsorption.[28–30] Furthermore, we demonstrate a correlation

between the ^{13}C chemical shift of methoxy surface intermediates, Lewis acid strength, and the CH_3OH formation rates of these materials. These trends indicate that the chemical shift of the methoxy species, formed as a surface intermediate during reaction, is an accurate descriptor of Lewis acid strength of M metal sites in this series of Cu-based CO_2 hydrogenation catalysts.

Results and Discussion

Catalyst synthesis and characterization

Cu nanoparticles supported on SiO_2, decorated with dispersed Hf, Nb, or Ta sites, were prepared using SOMC in two steps analogously to Cu/Ti@SiO_2[19] and Cu/Zr@SiO_2[18] materials that were previously reported (Scheme 1; the "M@SiO_2" nomenclature indicates a support composed of dispersed metal M sites on SiO_2; experimental details are included in the ESI, Section S1). First, isolated M sites, free of organic ligands, were generated on SiO_2 (dehydroxylated at 973 K, 10^{-3} Pa) by grafting a molecular precursor, $M(OSi(O^tBu)_3)_m(O^iPr)_n$ (where M = Ti [m = 3, n = 1], Zr [m = 4, n = 0], Hf [m = 4, n = 0], Nb [m = 3, n = 2], or Ta [m = 3, n = 2]), followed by thermal treatment under vacuum (10^{-3} Pa, 773 K), which removed organic ligands and simultaneously re-generated hydroxyl groups on the material. In the second step (Scheme 1b), Cu nanoparticles were generated on M@SiO_2 materials by grafting the copper precursor, $[Cu(O^tBu)]_4$ onto these M@SiO_2 materials, followed by a thermal treatment under H_2 flow (0.83 $cm^3\ s^{-1}\ g^{-1}$, 773 K). To allow accurate comparison among materials, the molar density of M on SiO_2 (~0.1 mmol g^{-1}) and the M/Cu molar ratio (~0.16) were held constant. The characterization data for these catalysts are shown in Table 1.

Each step of the grafting procedure was assessed using infrared (IR) spectroscopy of the solids, shown here for Hf@SiO_2 and Cu/Hf@SiO_2 as the representative material (Figure 1a). IR spectra of the dehydroxylated SiO_2 at 973 K (~1 OH nm^{-2} SiO_2, measured by quantification of released toluene after contacting the SiO_2 with $Mg(CH_2Ph)_2(THF)_2$); details in the ESI, Section S1) before and after contacting with the $Hf(OSi(O^tBu)_3)_4$ precursor solution indicate the initial presence of O-H stretching band at 3747 cm^{-1}, characteristic of isolated silanols, which decreases in intensity following contact with the Hf precursor solution. Solution ^1H nuclear magnetic resonance (NMR) spectroscopy of the decanted grafting solvent (using ferrocene as the internal standard) demonstrates the release of ~1 eq. of $HOSi(O^tBu)_3$ ligand per Hf (or Nb or Ta), indicating that grafting of the precursor occurs through protonolysis by the silanol groups of SiO_2. Consistent with this is the emergence of C-H stretching (2700-3100 cm^{-1}) and bending (1300-1500 cm^{-1}) bands of the solids after grafting (solids washed with solvent and dried under vacuum; ~10^{-3} Pa), which arise from the remaining organic ligands of the molecular precursor. Following thermal treatment (under vacuum (~10^{-3} Pa) at 773 K (0.083 K s^{-1}) for 5 h), these C-H bands are suppressed, indicating the removal of ligands, and the O-H bands re-emerge. Similar phenomena were observed for the Nb precursor (ESI, Figure S1a) and the Ta precursor (ESI, Figure S2a).

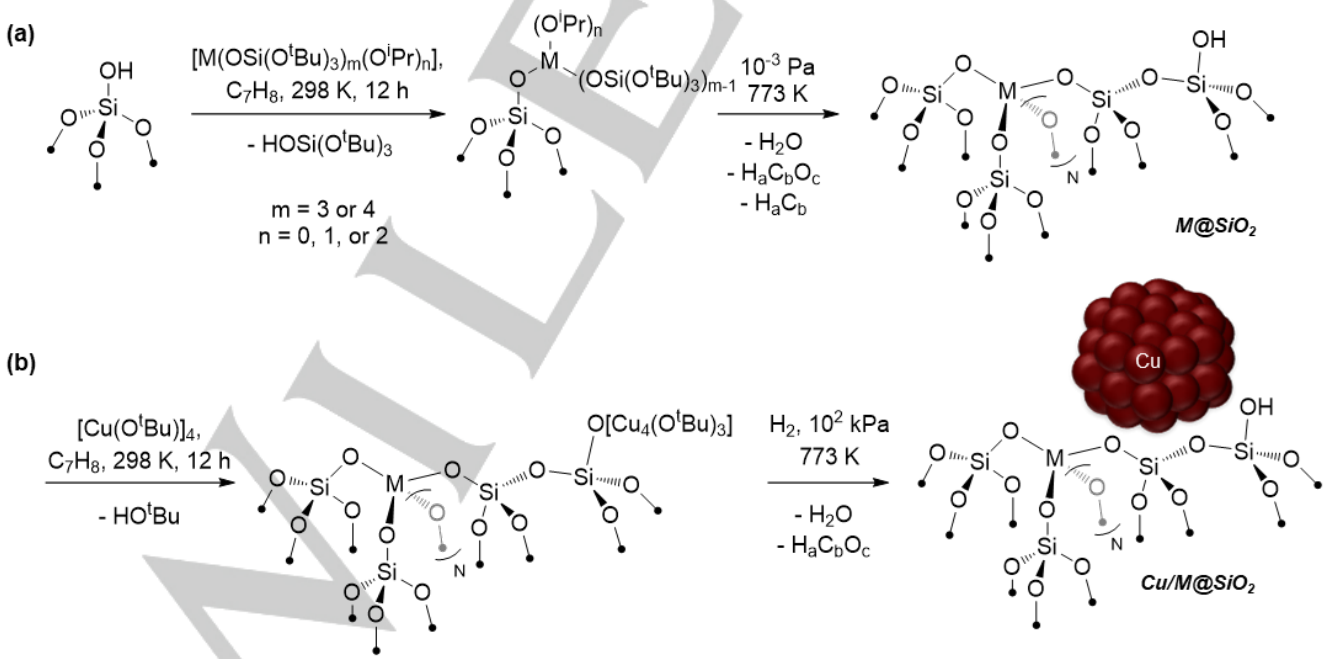

Scheme 1. Surface Organometallic Chemistry approach to generate **(a)** M@SiO_2 and **(b)** Cu/M@SiO_2, where M = Ti, Zr, Hf, Nb, or Ta. Details are included in the experimental section (ESI, Section S1).

10.1002/anie.202100672

Zr and Ti metal centers, dispersed on SiO_2 by the same approach,[18,19] were shown to be isolated Zr(IV) and Ti(IV) in these materials and even after Cu nanoparticles were generated on these tailored SiO_2 supports by grafting $[Cu(O^tBu)]_4$ followed by H_2 treatment. The Hf, Nb, and Ta metal sites for Hf@SiO_2, Nb@SiO_2, and Ta@SiO_2, prepared using analogous conditions, are also isolated and respectively Hf(IV), Nb(V), or Ta(V) in these materials, according to X-ray absorption spectroscopy (XAS; spectra, fits, and analysis for near edge and fine structure for M@SiO_2, Cu/M@SiO_2, and Cu/M@SiO_2 (spent) for M = Hf, Nb, and Ta, in ESI, Section S4). These findings are consistent with previous reports of grafted Hf(IV) and Nb(V) complexes on SiO_2 that also generated well-dispersed Hf(IV) and Nb(V) surface species.[31–33]

In the next step, $[Cu(O^tBu)]_4$ was grafted onto M@SiO_2 materials or SiO_2, and the resulting material was treated under H_2 flow (Scheme 1b). These steps were also monitored by IR spectroscopy (Figure 1b for Cu/Hf@SiO_2; Fig. S1b for Cu/Nb@SiO_2 and Fig. S2b for Cu/Ta@SiO_2), showing consumption of OH groups (v = 3747 cm^{-1}) with the concomitant appearance of C-H bands (v = 2700-3100 cm^{-1} and 1300-1500 cm^{-1}) upon grafting. Treatment under H_2 removes all organics, demonstrated by the disappearance of C-H bands, and restores the bands assigned to surface OH groups. The Cu nanoparticles on all materials are 2.7-2.9 nm in diameter (Table 1), according to transmission electron microscopy. Particle size distributions and sample micrographs are shown in Figure 1c and 1d for Cu/Hf@SiO_2 and are included in the ESI for Cu/Nb@SiO_2 and Cu/Ta@SiO_2 (Figure S4). Surface Cu sites (Cu_s) were determined by titration using N_2O pulses (assuming 1:2 N_2O:Cu stoichiometry); their values are similar for all materials except Cu/Ta@SiO_2 (43-55 mol g_{cat}^{-1}; Table 1), consistent with the nearly identical Cu particle sizes from TEM. For Cu/Ta@SiO_2, the size distribution of Cu nanoparticles is broader than for the other materials, with the observation of particles as small as 1 nm in diameter (Fig. S4). As a result of the larger surface-area-to-volume ratio of smaller nanoparticles, the Cu_s value from N_2O titrations is slightly greater for this material (66 mol g_{cat}^{-1}; Table 1) compared to the other Cu/M@SiO_2 catalysts (43-55 mol g_{cat}^{-1}; Table 1). In addition to Cu/M@SiO_2 (M = Ti, Zr, Hf, Nb, or Ta) materials, Cu/SiO_2 was synthesized using the same SOMC approach for comparison, with SiO_2 representing a support without Lewis acid M sites.

XANES spectra (ESI, Section S4) indicate that Lewis acid M sites retain their oxidation state, and EXAFS fits (ESI, Section S4) indicate that these M sites remain isolated and with a first coordination sphere primarily composed of O and thus do not alloy with Cu nanoparticles. As further confirmation of the unadulterated state of the Cu nanoparticles, CO was used as a probe molecule. CO (3.5 Pa) was introduced to the self-supporting wafers in the IR cell (details in the experimental section), then IR spectra were recorded. The IR spectrum was also recorded following the evacuation of CO at room temperature. In all cases (spectra in ESI, Figure S7), only the stretching mode of atop-bound CO interacting with Cu(0) was observed (v = 2101 cm^{-1}, consistent with literature reports[34]) in the presence of 3.5 Pa CO. This band is nearly identical to that for CO adsorbed to Cu/SiO_2, both in frequency (v = 2101-2110 cm^{-1}) and band width (FWHM = 40.9 ± 1.9 cm^{-1}), indicating that the Cu nanoparticles are unaffected by the presence of isolated metal centers on SiO_2. Following evacuation, the CO features disappeared for all materials, as expected for the reversible adsorption of CO on Cu(0) clusters.[35] These results indicate that the Cu nanoparticles were not detectably perturbed by the presence of isolated M sites dispersed on SiO_2.

The SOMC approach has produced a series of catalysts composed of identical Cu nanoparticles dispersed on tailored supports—M@SiO_2—that differ only in the identity of the dispersed group IV and V metal centers and, thus, in Lewis acid strength (vide infra). These materials thereby permit an accurate assessment of the effects of Lewis acid strength on CO_2 hydrogenation reactions.

Table 1. Characterization of Cu/M@SiO_2 catalysts

Catalyst	Composition / wt%		M/Cu atomic ratio	Cu_s / µmol g_{cat}^{-1} [b]	Cu particle size / nm [c]	CO vibrational frequency / cm^{-1} [d]
	Cu	M [a]				
Cu/Ti@SiO_2	4.0	0.48	0.16	44	2.8 ± 0.6	2102
Cu/Zr@SiO_2	4.4	0.98	0.15	50	2.8 ± 0.5	2103
Cu/Hf@SiO_2	4.6	2.2	0.17	51	2.9 ± 0.5	2101
Cu/Nb@SiO_2	3.8	0.92	0.17	43	2.7 ± 0.6	2104
Cu/Ta@SiO_2	4.5	2.2	0.17	66	2.6 ± 1.1	2110
Cu/SiO_2	4.6	--	--	55	2.9 ± 0.4	2101

[a] M = Ti, Zr, Hf, Nb, or Ta. [b] from N_2O titration. [c] from TEM; sample micrographs and particle size distributions for Cu/Hf@SiO_2 in Fig. 1c and 1d and for Cu/Nb@SiO_2, and Cu/Ta@SiO_2 included in the ESI, Fig. S3. [d] 3.5 Pa CO, 298 K. IR spectra included in the ESI, Fig. S7.

10.1002/anie.202100672

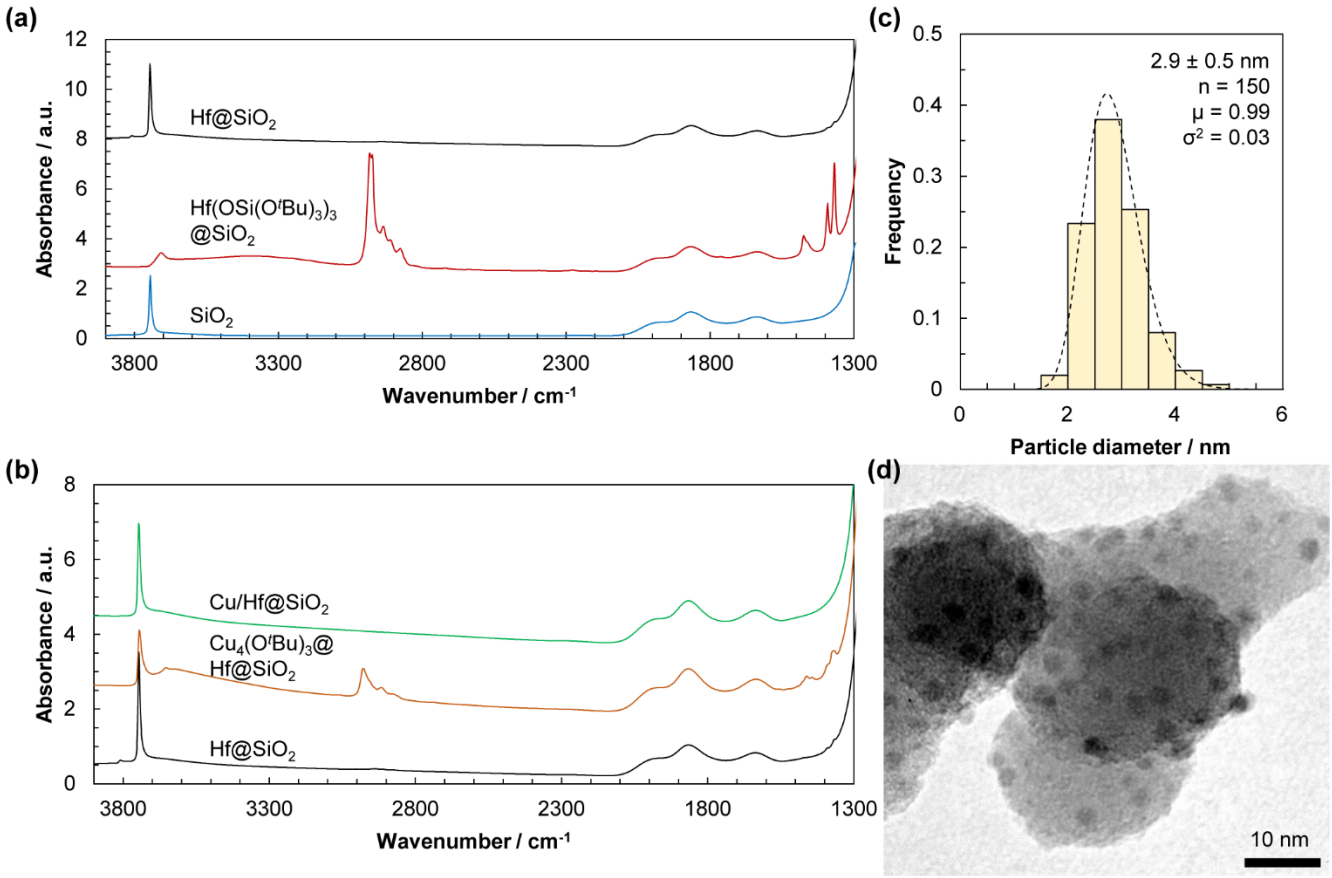

Figure 1. IR spectra throughout the synthesis of **(a)** Hf@SiO_2 (bottom: SiO_2 treated at 973 K; middle: SiO_2 after contacting with a solution of Hf(OSiO^{t}Bu)$_4$ and drying; top: Hf@SiO_2 after thermal treatment under vacuum) and **(b)** Cu/Hf@SiO_2 (bottom: Hf@SiO_2; middle: Hf@SiO_2 after contacting with a solution of [Cu(O^{t}Bu)]$_4$ and drying; top: Cu/Hf@SiO_2 after thermal treatment under H_2 flow). Details are included in the experimental section (ESI, Section S1). **(c)** Particle size distribution and **(d)** sample micrograph for Cu/Hf@SiO_2. Inset values in (c) are parameters for regression of the log-normal distribution.

CO_2 hydrogenation activity and selectivity

With these catalysts in hand, we evaluated their catalytic performance in CO_2 hydrogenation. The rates and product selectivities were measured at various CO_2 residence times for all materials (0.2-12 s g_{Cu} μmol^{-1}; 0.52 MPa CO_2, 1.56 MPa H_2, total pressure 2.6 MPa, 503 K; details in the ESI, Section S1), where CO and CH_3OH form through parallel pathways from reactant CO_2 (summarized in Scheme S1).[36–39] CH_3OH formation rates (Fig. S6) for all materials were greatest at the shortest residence times; as residence times increased, CH_3OH formation rates decreased precipitously for Cu/M@SiO_2 (where M = Ti, Zr, Hf, Nb, or Ta) and only slightly (by 10%) for Cu/SiO_2. CH_3OH formation rates were thus extrapolated to zero residence time to permit accurate comparison among catalysts (Fig. 2; Table 2). CH_3OH molar selectivities were also extrapolated to zero residence times, while CO formation rates, which were nearly insensitive to residence time, were averaged and are included in Table 2.

Initial CH_3OH formation rates are highest for Cu/Ti@SiO_2 (18.1 μmol (g_{Cu} s)$^{-1}$) then decrease as the heteroatom dispersed on SiO_2 changes from Nb to Ta to Zr to Hf (15.1 to 12.7 to 12.1 to 10.1 μmol (g_{Cu} s)$^{-1}$, respectively). In all cases, initial CH_3OH formation rates are more than 2-fold greater than for Cu/SiO_2 (3.61 μmol (g_{Cu} s)$^{-1}$), indicating that all of these group IV and V metal centers dispersed on SiO_2 promote CH_3OH formation. In contrast to these observed differences in CH_3OH formation rates among M-containing materials, the initial CO formation rates for all materials are similar and nearly identical to those for Cu/SiO_2 (2.95-3.47 μmol (g_{Cu} s)$^{-1}$ for Cu/M@SiO_2; 3.8 μmol (g_{Cu} s)$^{-1}$ for Cu/SiO_2). These results suggest that these reactions occur on the same types of sites and are consistent with previous observations that (reverse) water-gas-shift reactions occur on Cu surfaces.[37,40–42] Consequently, initial CH_3OH molar selectivities are greater for Cu/M@SiO_2 materials (77-85%) compared to Cu/SiO_2 (49%). Molar selectivity is greatest for Cu/Ti@SiO_2 (85%) and decreases slightly as Ti is replaced with Nb, Ta, Zr, and Hf, respectively (from 82% to 77%). These trends reflect the same promotional effects of M@SiO_2 on CH_3OH formation rates.

These promotional effects are explored further by examining the effects of reactor residence time on individual product formation rates. CO and CH_3OH formation rates on Cu/SiO_2 (Fig. S8f) are nearly independent of residence time. For Cu/SiO_2, the support can be considered innocent and Cu nanoparticles are likely the dominant active site for catalysis. CO formation rates for all

10.1002/anie.202100672

Cu/M@SiO_2 materials, normalized by mass of Cu, are similar in value (~ 3.2 μmol (g_{Cu} s)$^{-1}$) and nearly constant, irrespective of both residence time and catalyst identity (Fig. 2; Fig. S8). Furthermore, their values are similar to those for Cu/SiO_2 (3.78 μmol (g_{Cu} s)$^{-1}$), suggesting that these reactions occur on the same active site as those for Cu/SiO_2 and that CO is not an intermediate to form CH_3OH (consistent with previous reports[36–42]). In contrast, CH_3OH formation rates on Cu/M@SiO_2 decrease precipitously (by 20-30% as residence time increases 2-fold) with increasing residence time (Fig. S8), in spite of the low value of CO_2 conversion (< 7%). These trends cannot be explained by invoking the same active site as for Cu/SiO_2, because the rates of reactions catalyzed by such active sites (i.e., both CO and CH_3OH formation rates over Cu/SiO_2 and CO formation rates over Cu/M@SiO_2) are essentially independent of residence time. These residence time effects on CH_3OH formation rates for Cu/M@SiO_2 suggest the presence of two different active sites for these materials: the first is likely the same as for Cu/SiO_2 and is responsible for the formation of CO, and the second is unique to Cu/M@SiO_2 and is the active site for the formation of CH_3OH.

To further investigate the nature of this latter active site, the catalytic performance of M@SiO_2 and physical mixtures of M@SiO_2 with Cu/SiO_2 were assessed (Table S13). Concentrations of products were below detection limits for all M@SiO_2, indicating that these dispersed metal sites alone are not capable of catalyzing CO_2 hydrogenation. Each physical mixture of M@SiO_2 and Cu/SiO_2 yielded the same product formation rates and selectivities as Cu/SiO_2 alone. These results suggest a requirement for site proximity between the M sites and the Cu nanoparticles. Consequently, the active sites (or regions) for CH_3OH formation over Cu/M@SiO_2 are likely composed of adjacent Cu and M atoms, at the periphery of Cu nanoparticles. Similar active sites that interface metal nanoparticles and metal oxide supports have been invoked in a variety of catalytic reactions.[13–15,43,44]

Noteworthy is the challenge in assessing the proximity between M atoms and Cu nanoparticles by spectroscopic or microscopic methods. For example, M-O-Cu paths in EXAFS fitting (ESI, Section S4) could not be fit, but the small scattering features at greater distances could arise from Cu nanoparticles. Nevertheless, the use of SOMC to generate isolated metal sites and/or metal nanoparticles involves the grafting of metal precursors onto isolated silanols, which are likely statistically distributed (~1 OH/nm^{-2}).[22] SOMC generates highly dispersed metal sites or metal nanoparticles upon thermal treatments, as evidenced by EXAFS (ESI, Section S4) and microscopy (Fig. 1c-d and ESI, Fig. S3), respectively. Consequently, the random distribution of M sites and Cu nanoparticles across the SiO_2 surface results in each Cu nanoparticle being near at least one M site. The proximity of these M sites and Cu nanoparticles is further corroborated by the observed promotional effects on CH_3OH formation rates and selectivities for these catalysts, while physical mixtures of M@SiO_2 and Cu/SiO_2 behave as Cu/SiO_2 alone (vide supra). These findings are also consistent with reaction pathways determined using density functional theory calculations for Cu-based materials on crystalline ZrO_2 and Al_2O_3 supports.[17,46] Sites at the interface of Cu nanoparticles and the Lewis acid support were shown to not only promote the activation of CO_2 but also to stabilize reaction intermediates such as formate and methoxy surface species, compared to pathways catalyzed by Cu surfaces alone. Additionally, although CO_2 could be activated by the Lewis acid sites of the support alone, methanol formation does not occur in the absence of Cu nanoparticles.

The increases in CH_3OH rates and selectivities arising from these isolated group IV and V metal centers on SiO_2 can therefore be attributed to their role as Lewis acid sites, which have previously been demonstrated to stabilize electron-rich formate and methoxy surface intermediates.[17–20] These interfacial sites here result in the observed decreases in CH_3OH formation rate with increasing residence time because products formed during these reactions (i.e., H_2O or CH_3OH) competitively adsorb onto these Lewis acid sites. Next, we measure Lewis acid strength for M@SiO_2 and examine the stabilization of surface intermediates.

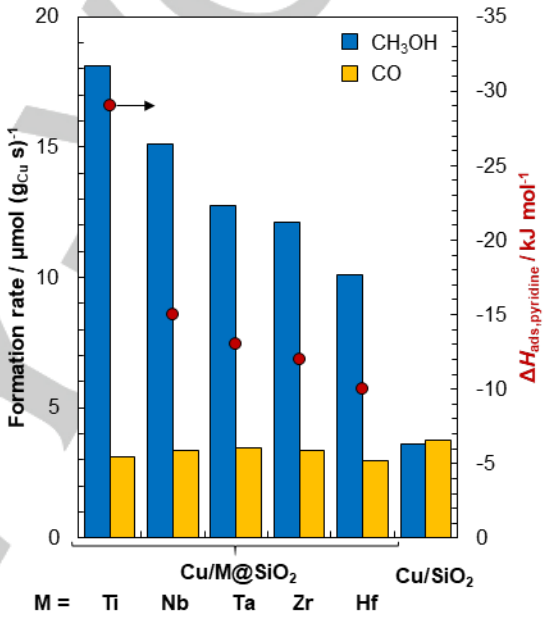

Figure 2. CH_3OH (blue; left axis) and CO (yellow; left axis) formation rates (0.52 MPa CO_2, 1.56 MPa H_2, 2.6 MPa, 503 K; extrapolated to zero residence time) and enthalpies of pyridine adsorption to the M atoms on M@SiO_2 ($\Delta H_{ads,pyridine}$; right axis) for Cu/M@SiO_2 (M = Ti, Nb, Ta, Zr, or Hf) and Cu/SiO_2.

Table 2. Initial CH_3OH and CO formation rates and CH_3OH molar selectivities.

Catalyst	Initial CH_3OH formation rate / μmol (g_{Cu} s)$^{-1}$ [a]	Initial CO formation rate / μmol (g_{Cu} s)$^{-1}$ [b]	Initial CH_3OH molar selectivity [c]
Cu/Ti@SiO_2	18.1 ± 0.6	3.12 ± 0.04	85 ± 4 %
Cu/Nb@SiO_2	15.1 ± 0.2	3.36 ± 0.16	82 ± 1 %
Cu/Ta@SiO_2	12.7 ± 0.1	3.47 ± 0.01	79 ± 2 %
Cu/Zr@SiO_2	12.1 ± 0.2	3.37 ± 0.02	78 ± 2 %
Cu/Hf@SiO_2	10.1 ± 0.1	2.95 ± 0.06	77 ± 1 %
Cu/SiO_2	3.61 ± 0.14	3.78 ± 0.03	49 ± 2 %

[a] error represents 95% confidence interval. [b] error represents standard error. [c] error represents 95% confidence interval.

Measures of Lewis acid strength

The enthalpy of adsorption for pyridine, a molecule with a lone pair of electrons that interact with electrophilic Lewis acid sites and whose interaction has been widely studied,[26,28,45] was measured. Pyridine adsorption enthalpies ($\Delta H_{ads,pyridine}$) were determined from pyridine isobars (0.1 kPa, 483-523 K) using IR spectroscopy (spectra at 483 K included in the ESI, Figure S10a, for M@SiO_2 materials) by evaluating the area of the pyridine vibrational band at 1450 cm^{-1} and regressing these values to the van't Hoff equation (isobars in the ESI, Fig. S10b). Heats of adsorption were assessed using M@SiO_2 because of the presence of an additional vibration band at 1444 cm^{-1} for Cu/M@SiO_2; the area and the FWHM of the 1450 cm^{-1} bands are nearly identical for each M@SiO_2 compared to its respective Cu/M@SiO_2 material after subtraction of the band at 1444 cm^{-1} (ESI, Section S8), indicating that pyridine adsorption on M sites is otherwise unaffected by the presence of Cu nanoparticles. The values of these adsorption enthalpies ($\Delta H_{ads,pyridine}$) are shown in Fig. 2 (right axis; values in the ESI, Table S15). The $\Delta H_{ads,pyridine}$ value is most negative for Ti, indicating that the interaction of pyridine with isolated Ti sites is the most exothermic among M sites. Thus, Ti is the strongest Lewis acid among those considered here, and Lewis acid strength of the metal sites decrease in the order: Ti > Nb > Ta > Zr > Hf, with Hf having the least negative $\Delta H_{ads,pyridine}$ value and therefore the lowest acid strength.

Notably, the initial CH_3OH formation rates and CH_3OH selectivities increase as $\Delta H_{ads,pyridine}$ values become more negative (Fig. 2). This observed relationship suggests that surface intermediates and transition states that are unique to the reaction pathway for CH_3OH formation (and not CO formation) are preferentially stabilized by interfacial Lewis acid M sites. To investigate the identity of surface intermediates formed, Cu/M@SiO_2 materials were treated ex situ (exposed to a gas mixture of $^{13}CO_2$:H_2 1:3 molar ratio, 0.6 MPa, 503 K, 12 h), then analyzed by solid-state NMR. Correlation peaks for methoxy species ($\delta(^{13}C)/\delta(^{1}H)$ = 60 ppm/4.5 ppm and 49 ppm/3.7 ppm) are present in the ^{1}H-^{13}C HETCOR spectrum of Cu/Ta@SiO_2 (Fig. 3a), shown as a representative example. ^{1}H-^{13}C HETCOR spectra of Cu/Ti@SiO_2 and Cu/Zr@SiO_2 have been previously reported (in [19] and [18], respectively) and also include correlation peaks for formate species ($\delta(^{13}C)/\delta(^{1}H)$ = 170 ppm/8 ppm). Solid state CP-MAS NMR spectra of all ex situ treated Cu/M@SiO_2 materials demonstrate the presence of methoxy and/or adsorbed CH_3OH ($\delta(^{13}C)$ = 49-65 ppm) species (Fig. 3b). Specifically, two methoxy groups are detected, with the downfield signal likely directly connected to the metal sites, while the one at 49 ppm can be interpreted as an adsorbed CH_3OH or a methoxy bound to Si (vide infra). Spectra for all materials except Cu/Ta@SiO_2 and Cu/Hf@SiO_2 also show formate species ($\delta(^{13}C)$ = 170-172 ppm). In comparison, only a very weak and broad signal ($\delta(^{13}C)$ = 168 ppm), which was attributed to formate adsorbed to Cu nanoparticles, was detected for Cu/SiO_2 that was treated under the same conditions.[17] Overall, the intense features for observed Cu/M@SiO_2 materials indicate that methoxy and formate species are chemisorbed on the Lewis acid M sites. These data clearly suggest that the surface reaction intermediates are stabilized by these Lewis acid sites for all Cu/M@SiO_2 materials, in a manner correlated with their Lewis acid strength. The stabilization of surface intermediates by these M atoms is beneficial for CH_3OH formation rates, in contrast to a previous report of strongly Lewis acidic Al_2O_3 adsorbing formate intermediates too strongly.[46] This over-stabilized formate further reacts with CH_3OH, leading to the formation of methyl formate and its subsequent decomposition to CO (and CH_3OH) and therefore higher CO selectivity.

Examining the methoxy/CH_3OH species in the NMR spectra (49-65 ppm, Fig. 3b) reveals that for all materials except Cu/Hf@SiO_2, there are at least two distinct ^{13}C chemical shifts ($\delta(^{13}C)$). One feature is uniformly observed at 49 ppm, and the predominant second signal occurs at greater chemical shift than the first. The downfield shift of this latter peak, compared to the one at 49 ppm, depends on the surface M Lewis acid sites. For Cu/Hf@SiO_2, the sole observed signal is at a $\delta(^{13}C)$ value of 49 ppm and can be attributed either to coordinated CH_3OH or methoxy coordinated to Si. In contrast, for Cu/Ti@SiO_2, Cu/Nb@SiO_2, Cu/Ta@SiO_2, and Cu/Zr@SiO_2, the predominant additional signal appears at $\delta(^{13}C)$ = 65, 63, 59, and 53 ppm, respectively (the deconvolution of spectrum for Cu/Zr@SiO_2 is shown in the ESI, Figure S11). This downfield signal is specific to the presence of the M Lewis acid sites and parallels what is observed for the corresponding molecular methoxide compounds. Specifically, for Ti, Nb, and Ta molecular methoxides, $\delta(^{13}C)$ values are greatest for Ti ($\delta(^{13}C)$ = 61 and 77 ppm for $[Ti(OCH_3)_4]_2$) then decrease for Nb ($\delta(^{13}C)$ = 61.1 and 60 ppm for $[Nb(OCH_3)_5]_2$ in C_6D_6) and for Ta ($\delta(^{13}C)$ = 59.6 ppm for $[Ta(OCH_3)_5]_2$ in C_6D_6). The ^{13}C NMR spectra for these are included in the ESI (Fig. S31, S26, and S30, respectively).

The assignment of the downfield signals as methoxy coordinated to M Lewis acid sites was corroborated (Fig. S12) using density functional theory (DFT)-optimized molecular models (e.g., $Ti(OCH_3)_4$, $[Ti(OCH_3)_4]_2$, CH_3OH, and CH_3OH coordinated to $Ti(OCH_3)_4$). These were used to obtain values of the isotropic chemical shift, $\delta_{iso,calc}$ (DFT methods and calculation of $\delta_{iso,calc}$ are discussed in the ESI, Section S9), which are similar to measured values (ESI, Fig. S12). It is noteworthy that the measured $\delta(^{13}C)$ values of these surface methoxy species (denoted as $\delta_{iso,exp}$) decrease from Ti (65 ppm) to Nb (63 ppm) to Ta (59 ppm) to Zr (53 ppm) to Hf (49 ppm; note the varied possible attribution, vide supra), a trend that parallels what is observed for both intrinsic CH_3OH formation rates on these materials and $\Delta H_{ads,pyridine}$ values (Fig. 2). Understanding this relationship, which ultimately reflects the stabilization of these methoxy intermediates by Lewis acid sites (vide infra), requires interpreting the measured ^{13}C chemical shift ($\delta_{iso,exp}$) to determine its electronic origins.

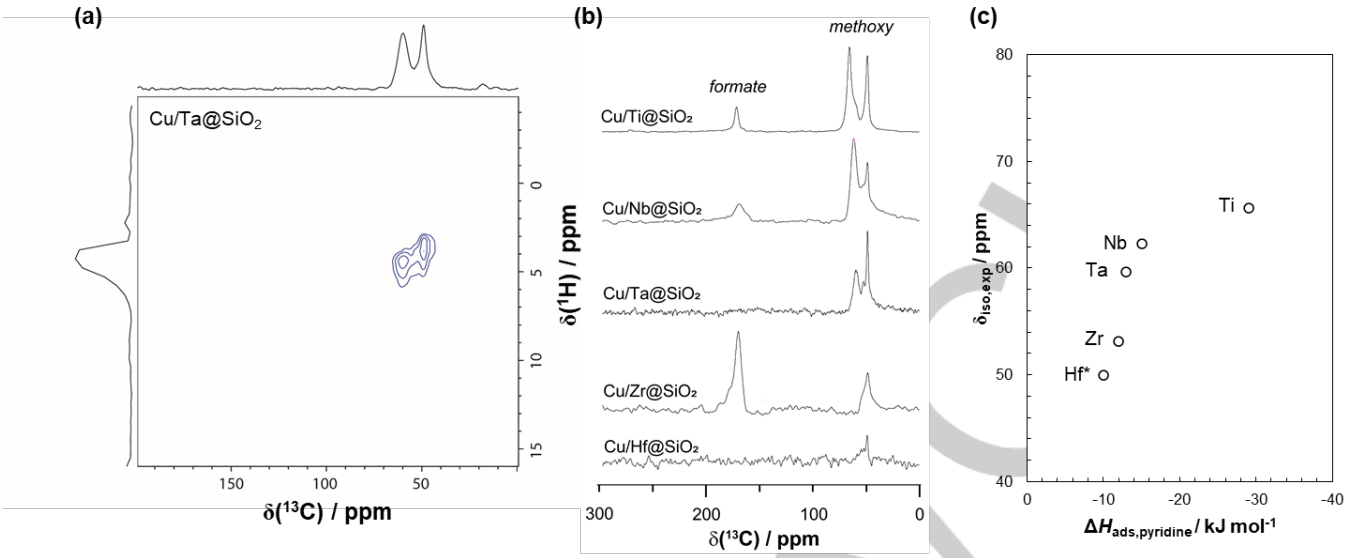

Figure 3. (a) ^{1}H-^{13}C HETCOR spectrum of Cu/Ta@SiO_2 after reaction with $^{13}CO_2$ and H_2 (0.6 MPa, 3:1 H_2:$^{13}CO_2$, 503 K, 12 h) showing the correlation peaks for methoxy species. **(b)** CP-MAS NMR ^{13}C spectra of Cu/M@SiO_2, after reaction with $^{13}CO_2$ and H_2 (0.6 MPa, 3:1 H_2:$^{13}CO_2$, 503 K, 12 h). **(c)** Measured ^{13}C chemical shifts ($\delta_{iso,exp}$) for M-OCH_3 as a function of the enthalpy of adsorption for pyridine on the M-atom ($\Delta H_{ads,pyridine}$).
*For Hf, the chemical shift for the sole measured signal in the CH_3OH/OCH_3 region (48-66 ppm) is likely either Si-OCH_3 or adsorbed CH_3OH. (see ESI, Section S9 for details).

The isotropic chemical shift (δ_{iso}) is the average of the three principal components (δ_{ii}) of the chemical shift tensor ($\delta_{iso} = \sum_{i=1}^{3} \delta_{ii}/3$), which are related to the principal components of the chemical shielding tensor (σ_{ii}) by difference from a reference ($\delta_{ii} \approx \sigma_{iso,ref} - \sigma_{ii}$, where $\sigma_{iso,ref}$ is the chemical shielding tensor for the reference compound). The chemical shielding tensor can be further divided into paramagnetic (σ_{para}) and diamagnetic (σ_{dia}) contributions ($\sigma_{iso} = \sigma_{para} + \sigma_{dia}$), where the latter originate from the core orbitals and are therefore rather insensitive to changes in electronic environment. The paramagnetic contributions (σ_{para}) are, in contrast, sensitive to the frontier orbitals (i.e., the orbitals including and near the HOMO and the LUMO).[47] Natural chemical shielding (NCS) analysis allows the attribution of the electronic origin of chemical shifts by deconvoluting chemical shielding to contributions of frontier orbitals,[48] examined here using small cluster models as structural analogs of surface species for M@SiO_2 via DFT methods (CH_3O-Ti@SiO_2 is shown in Figure 4a; all cluster models are shown in the ESI, Fig. S13). Specifically, by comparing the trends in each chemical shielding component across a series of structures and by examining the orientation of the chemical shielding tensor (the axes in Fig. 4a for CH_3O-Ti@SiO_2 and in the ESI, Fig. S15), the electronic origins of the chemical shielding, and therefore chemical shifts, can be determined. The entirety of the results and a complete discussion of NCS analysis are included in the ESI (Section S9), and the findings are summarized next.

NCS analysis reveals that the measured changes in $\delta_{iso,exp}$ values primarily originate from the paramagnetic contributions to two of the principal components of chemical shielding: $\sigma_{11,para}$ and $\sigma_{22,para}$. These paramagnetic contributions are further deconvoluted into the individual natural localized molecular orbital (NLMO) contributions. The decomposition of $\sigma_{11,para}$ for CH_3O-Ti@SiO_2 and CH_3O-Hf@SiO_2 into NLMO contributions are shown in Figure 4b as illustrative examples (all results are in the ESI, Section S9).

Comparison among all CH_3O-M@SiO_2 indicates that the primary contribution to $\sigma_{11,para}$, which remains constant for all M, is the σ(C-O) orbital (C-O NLMO shown by the yellow bar, Fig. 4b). The second greatest contribution, which varies among CH_3O-M@SiO_2 (Fig. S16), is that of the C-H bonding NLMO (light blue bar, Fig. 4b), which corresponds to the π(CH_3) molecular orbitals. The change in paramagnetic contributions as M sites vary arises from the coupling of the π(CH_3) orbital with the low-lying σ*(C-O) orbital, as schematically depicted in Figure 4c. This coupling decreases in the order: Ti, Nb, Ta, Zr, to Hf, as a result of the increasing energy difference between the π(CH_3) and σ*(C-O) orbitals (denoted $\Delta E_{virt.-occ}$ in Fig. 4c).

This energy difference ($\Delta E_{virt.-occ}$) is largely a result of the energy of the σ*(C-O) orbital (Fig. 4c), which decreases as the M-O bonding interaction becomes stronger (i.e., M=O). That is, a decrease in energy of empty d-orbitals in these d^0 M (Lewis acid) sites, which have the appropriate symmetry to accept electron density from the lone pairs on the oxygen of the -OCH_3 ligand (Lewis base). Taken together, these result in the decrease in the energy of the σ*(C-O) orbital (Fig. 4c). Changes in the values of $\delta_{iso,exp}$ therefore reflect differences in the extent of charge transfer and the bonding energy of the -OCH_3 ligand to the M sites. These energy differences also indicate trends in the Lewis acid strength of these M sites, as reflected by the strong correlation with $\Delta H_{ads,pyridine}$ values (Fig. 3c). Thus, these measured δ(^{13}C) values for M-(OCH_3) species directly reflect energetic stabilization of methoxy surface intermediates through Lewis acid-base interactions that can be examined directly by measured values of $\delta_{iso,exp}$ or indirectly via $\Delta H_{ads,pyridine}$ (or the enthalpies of adsorption of other base titrants).

10.1002/anie.202100672

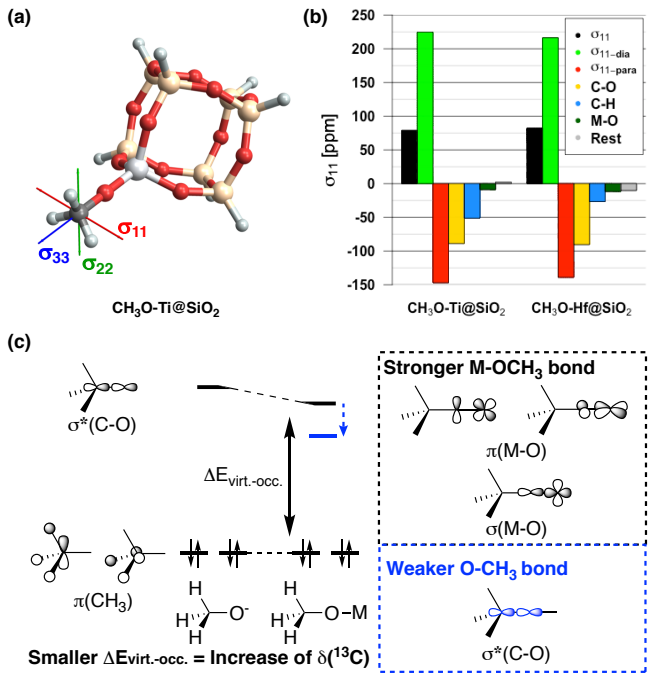

Figure 4. (a) Structure and chemical shielding tensor orientation (σ_{11}: red, σ_{22}: green, σ_{33}: blue) for the CH_3O-Ti@SiO_2 cluster model. **(b)** Decomposition of the principal chemical shielding component σ_{11} into $\sigma_{11\text{-dia}}$ and $\sigma_{11\text{-para}}$ and further into individual NLMO contributions for $\sigma_{11\text{-para}}$ for CH_3O-Ti@SiO_2 and CH_3O-Hf@SiO_2. **(c)** Scheme of the effects of Lewis acid strength on orbital energies; the decrease in the σ*(C-O) orbital energy leads to increased deshielding (details in ESI, Section S9).

Lewis acid strength and the promotion of CH_3OH formation rates

The same Lewis acid sites that stabilize surface intermediates also stabilize transition states. Examining such transition state stabilization requires measurement of rate constants, rigorously normalized by the number of active sites. Here, intrinsic CH_3OH formation turnover rates (per M atom) can be taken as a surrogate for rate constants because reactant pressures were held constant and rates were extrapolated to zero residence time. These turnover rates increase with increasing $\delta_{iso,exp}$ values (Figure S32a) and as pyridine adsorption enthalpies become less negative (Figure S32b). Importantly, the exponential increase in turnover rates as $\Delta H_{ads,pyridine}$, the energetic functional descriptor of Lewis acid strength, becomes more negative reflects the greater stabilization of transition states as Lewis acid strength increases. These results indicate the crucial role that Lewis acid sites have in stabilizing surface intermediates at the periphery of Cu nanoparticles.

Notable is the ability to characterize the Lewis acid strength of these d^0 metals by examining $\delta(^{13}C)$ values of surface intermediates formed during reaction, because to date the characterization of Lewis acid strength has required the use of probe molecules (Lewis bases) that are typically unrelated to the reaction being investigated. For example, IR spectroscopy and NMR spectroscopy of adsorbed pyridine,[26,45] trialkylphosphine[49] or trialkylphosphine oxides,[50,51] acetonitrile,[29] and CO[52] have been used to garner information about acid strength by examining changes in vibrational frequencies or chemical shifts or desorption temperatures. However, the inferred strength of a Lewis acid site from such methods is sensitive to the identity of the probe molecule as a result of the electrostatic and steric interactions at the Lewis acid-base pair.[53,54] Furthermore, the use of probe molecules can alter the catalyst through structural deformation or charge reorganization[54] and result in misleading or poorly attributed structure-function relations. Here, the ^{13}C chemical shifts of methoxy surface intermediates are demonstrated to be a powerful descriptor for rates of conversion of CO_2 to CH_3OH. This is because, in contrast to unrelated probe molecules, the $\delta_{iso,exp}$ values directly assess the stability of a surface species that resides along the reaction coordinate at a position near kinetically relevant transition states for this reaction. No other probe molecule could more closely resemble a surrogate for the active complexes that determine rates of CH_3OH formation. Thus, the stabilization of these intermediates by the increasing strength of M surface sites reflects the precise stabilization afforded by Lewis acid sites for CO_2 hydrogenation to CH_3OH.

These $\delta(^{13}C)$ values for these methoxy intermediates provide a general measure of Lewis acid strength, even when unrelated to the catalyzed reaction of interest. However, in those cases, these chemical shifts suffer from the same problems as other external probe molecules. The most insightful measures of Lewis acid strength require the use of a probe molecule that is an intermediate along the reaction coordinate for the catalytic reaction of interest. A related strategy was used in the investigation of alkene epoxidation reactions on Lewis acid BEA zeotypes.[55,56] The epoxide product of these reactions was used as the probe molecule to examine the oxygen transfer elementary step. Isothermal titration calorimetry allowed the simultaneous examination of the stabilization of the product state for that specific elementary step and a functional measure of differences between the Lewis acid strength caused by changes in the elemental identity of the transition metal present in the framework or the density of silanol defects and presence of water. Thus, for multi-step reaction networks generally, the most insightful measurements of the chemical nature of active sites will come from experimental measurements (e.g., NMR or ITC) that utilize as probe molecules the reactive and surface intermediates that participate directly in the elementary steps of the catalytic cycle.

Conclusion

The synthesis of a series of analogous catalysts containing Cu nanoparticles supported on SiO_2 decorated with metal centers of different Lewis acid strength (Cu/M@SiO_2, where M = Ti, Zr, Hf, Nb, Ta) was enabled by using a SOMC approach. CO formation rates on these materials were nearly identical and independent of residence time. In contrast, CH_3OH formation rates varied as a function of the identity of the M atom. The promotion of CH_3OH formation rates and selectivities reflect their increasing acid strength, described here by measuring pyridine adsorption enthalpies for these metal centers as well as by the ^{13}C chemical shift of methoxy surface intermediates from solid-state NMR. These findings indicate that the Lewis acid M sites of these catalysts stabilize surface intermediates (formate and methoxy) at the periphery of Cu nanoparticles to promote CH_3OH formation

rates. This study also establishes the ^{13}C chemical shift of the methoxy surface intermediates as a measure of Lewis acid strength and as an informative descriptor of the reactivity in CO_2 hydrogenation to CH_3OH. The molecular origin of this correlation between chemical shift and Lewis acid strength is revealed to be a result of the nature of the M–OCH_3 bond. Specifically, the presence of a low energy d-orbital of appropriate symmetry in the M Lewis acid sites can generate π-bond character in the M–O bond of the M-OCH_3 and thereby affect the $\delta(^{13}C)$ of these methoxy surface intermediates; such methoxy intermediates are readily measured and calculated but importantly report directly on the Lewis acid strength of the metal sites and the stabilization of these intermediates. Moreover, the same stabilization of intermediates by Lewis acid sites likely results in the stabilization of transition states for the formation of CH_3OH, demonstrating the chemical origin of promotional effects.

This study highlights how the SOMC approach can be used to develop tailored catalyst systems that allow interrogation of the effects of individual promoters with molecular level precision, in order to provide structure-function relations toward the development of catalysts as exemplified here for the selective hydrogenation of CO_2 to CH_3OH.

Acknowledgments

We thank Dr. Olga Safonova for XAS measurements at the Paul Scherrer Institute (SuperXAS); Lukas Rochlitz (ETHZ) for transmission electron microscopy; and Christian Ehinger and Christopher P. Gordon (ETHZ) for discussion regarding NCS analysis. G.N., E.L., and P.S. were supported by the SCCER-Heat and Energy Storage program of InnoSuisse. D.T.B. and D.W.F. were supported by the U.S. Army Research Office (W911NF-18-1-0100).

Keywords: CO_2 hydrogenation • surface organometallic chemistry • CH_3OH synthesis • heterogeneous catalysis • Lewis acids

[1] G. A. Olah, A. Goeppert, G. K. S. Prakash, *Beyond Oil and Gas*, Wiley-VCH Verlag GmbH & Co. KGaA, Weinheim, Germany, **2018**.

[2] G. A. Olah, *Angew. Chemie Int. Ed.* **2013**, *52*, 104–107; *Angew. Chemie* **2013**, *125*, 112-116.

[3] A. Álvarez, A. Bansode, A. Urakawa, A. V. Bavykina, T. A. Wezendonk, M. Makkee, J. Gascon, F. Kapteijn, *Chem. Rev.* **2017**, *117*, 9804–9838.

[4] C. Schild, A. Wokaun, A. Baiker, *J. Mol. Catal.* **1990**, *63*, 223–242.

[5] I. A. Fisher, H. C. Woo, A. T. Bell, *Catal. Letters* **1997**, *44*, 11–17.

[6] J. A. Rodriguez, P. Liu, D. J. Stacchiola, S. D. Senanayake, M. G. White, J. G. Chen, *ACS Catal.* **2015**, *5*, 6696–6706.

[7] J. Graciani, K. Mudiyanselage, F. Xu, A. E. Baber, J. Evans, S. D. Senanayake, D. J. Stacchiola, P. Liu, J. Hrbek, J. F. Sanz, J. A. Rodriguez, *Science (80-.).* **2014**, *345*, 546–550.

[8] S. Kattel, B. Yan, Y. Yang, J. G. Chen, P. Liu, *J. Am. Chem. Soc.* **2016**, *138*, 12440–12450.

[9] K. Chang, T. Wang, J. G. Chen, *Appl. Catal. B Environ.* **2017**, *206*, 704–711.

[10] J. Kim, B. B. Sarma, E. Andrés, N. Pfänder, P. Concepción, G. Prieto, *ACS Catal.* **2019**, *9*, 10409–10417.

[11] J. J. Corral-Pérez, C. Copéret, A. Urakawa, *J. Catal.* **2019**, 0–7.

[12] M. Behrens, *Angew. Chemie Int. Ed.* **2014**, *53*, 12022–12024; *Angew. Chemie* **2014**, *126*, 12216-12218.

[13] M. E. Witzke, P. J. Dietrich, M. Y. S. Ibrahim, K. Al-Bardan, M. D. Triezenberg, D. W. Flaherty, *Chem. Commun.* **2017**, *53*, 597–600.

[14] F. Dong, Y. Zhu, H. Zheng, Y. Zhu, X. Li, Y. Li, *J. Mol. Catal. A Chem.* **2015**, *398*, 140–148.

[15] Z. Strassberger, A. H. Alberts, M. J. Louwerse, S. Tanase, G. Rothenberg, *Green Chem.* **2013**, *15*, 768–774.

[16] I. Ro, J. Resasco, P. Christopher, *ACS Catal.* **2018**, *8*, 7368–7387.

[17] K. Larmier, W.-C. Liao, S. Tada, E. Lam, R. Verel, A. Bansode, A. Urakawa, A. Comas-Vives, C. Copéret, *Angew. Chemie Int. Ed.* **2017**, *56*, 2318–2323; *Angew. Chemie* **2017**, *129*, 2358.

[18] E. Lam, K. Larmier, P. Wolf, S. Tada, O. V. Safonova, C. Copéret, *J. Am. Chem. Soc.* **2018**, *140*, 10530–10535.

[19] G. Noh, E. Lam, J. L. Alfke, K. Larmier, K. Searles, P. Wolf, C. Copéret, *ChemSusChem* **2019**, *12*, 968–972.

[20] G. Noh, S. R. Docherty, E. Lam, X. Huang, D. Mance, J. L. Alfke, C. Copéret, *J. Phys. Chem. C* **2019**, *123*, 31082–31093.

[21] E. Lam, K. Larmier, S. Tada, P. Wolf, O. V. Safonova, C. Copéret, *Chinese J. Catal.* **2019**, *40*, 1741–1748.

[22] C. Copéret, *Acc. Chem. Res.* **2019**, *52*, 1697–1708.

[23] M. K. Samantaray, V. D'Elia, E. Pump, L. Falivene, M. Harb, S. Ould Chikh, L. Cavallo, J.-M. Basset, *Chem. Rev.* **2020**, *120*, 734–813.

[24] M. K. Samantaray, E. Pump, A. Bendjeriou-Sedjerari, V. D'Elia, J. D. A. Pelletier, M. Guidotti, R. Psaro, J.-M. Basset, *Chem. Soc. Rev.* **2018**, *47*, 8403–8437.

[25] R. J. Witzke, A. Chapovetsky, M. P. Conley, D. M. Kaphan, M. Delferro, *ACS Catal.* **2020**, *10*, 11822–11840.

[26] W. R. Gunther, V. K. Michaelis, R. G. Griffin, Y. Roman-Leshkov, *J. Phys. Chem. C* **2016**, *120*, 28533–28544.

[27] D. T. Bregante, A. Y. Patel, A. M. Johnson, D. W. Flaherty, *J. Catal.* **2018**, *364*, 415–425.

[28] D. T. Bregante, N. E. Thornburg, J. M. Notestein, D. W. Flaherty, *ACS Catal.* **2018**, *8*, 2995–3010.

[29] D. T. Bregante, D. W. Flaherty, *J. Am. Chem. Soc.* **2017**, *139*, 6888–6898.

[30] D. T. Bregante, A. M. Johnson, A. Y. Patel, E. Z. Ayla, M. J. Cordon, B. C. Bukowski, J. Greeley, R. Gounder, D. W. Flaherty, *J. Am. Chem. Soc.* **2019**, *141*, 7302–7319.

[31] A. Hamieh, R. Dey, B. Nekoueishahraki, M. K. Samantaray, Y. Chen, E. Abou-Hamad, J.-M. Basset, *Chem. Commun.* **2017**, *53*, 7068–7071.

[32] G. Tosin, C. C. Santini, A. Baudouin, A. De Mallman, S. Fiddy, C. Dablemont, J.-M. Basset, *Organometallics* **2007**, *26*, 4118–4127.

[33] N. E. Thornburg, A. B. Thompson, J. M. Notestein, *ACS Catal.* **2015**, *5*, 5077–5088.

[34] J. Pritchard, T. Catterick, R. K. Gupta, *Surf. Sci.* **1975**, *53*, 1–20.

[35] K. Hadjiivanov, H. Knözinger, *Phys. Chem. Chem. Phys.* **2001**, *3*, 1132–1137.

[36] E. L. Kunkes, F. Studt, F. Abild-Pedersen, R. Schlögl, M. Behrens, *J. Catal.* **2015**, *328*, 43–48.

[37] Y. Yang, C. A. Mims, D. H. Mei, C. H. F. Peden, C. T. Campbell, *J. Catal.* **2013**, *298*, 10–17.

[38] R. Gaikwad, H. Reymond, N. Phongprueksathat, P. Rudolf von

Rohr, A. Urakawa, *Catal. Sci. Technol.* **2020**, *10*, 2763–2768.

[39] A. Karelovic, G. Galdames, J. C. Medina, C. Yévenes, Y. Barra, R. Jiménez, *J. Catal.* **2019**, *369*, 415–426.

[40] Y. Yang, C. A. Mims, R. S. Disselkamp, J. Kwak, C. H. F. Peden, C. T. Campbell, *J. Phys. Chem. C* **2010**, *114*, 17205–17211.

[41] A. A. Gokhale, J. A. Dumesic, M. Mavrikakis, *J. Am. Chem. Soc.* **2008**, *130*, 1402–1414.

[42] N. Schumacher, A. Boisen, S. Dahl, A. Gokahle, S. Kandoi, L. Grabow, J. Dumesic, M. Mavrikakis, I. Chorkendorff, *J. Catal.* **2005**, *229*, 265–275.

[43] L. Foppa, T. Margossian, S. M. Kim, C. Müller, C. Copéret, K. Larmier, A. Comas-Vives, *J. Am. Chem. Soc.* **2017**, *139*, 17128–17139.

[44] J. J. Corral-Pérez, A. Bansode, C. S. Praveen, A. Kokalj, H. Reymond, A. Comas-Vives, J. VandeVondele, C. Copéret, P. R. von Rohr, A. Urakawa, *J. Am. Chem. Soc.* **2018**, *140*, 13884–13891.

[45] E. Parry, *J. Catal.* **1963**, *2*, 371–379.

[46] E. Lam, J. J. Corral-Pérez, K. Larmier, G. Noh, P. Wolf, A. Comas-Vives, A. Urakawa, C. Copéret, *Angew. Chemie Int. Ed.* **2019**, *58*, 13989–13996; *Angew. Chemie* **2019**, *131*, 14127-14134.

[47] J. Autschbach, S. Zheng, R. W. Schurko, *Concepts Magn. Reson. Part A* **2010**, *36A*, 84–126.

[48] J. A. Bohmann, F. Weinhold, T. C. Farrar, *J. Chem. Phys.* **1997**, *107*, 1173–1184.

[49] X. Yi, H. Ko, F. Deng, S. Liu, A. Zheng, *Nat. Protoc.* **2020**, *15*, 3527–3555.

[50] J. P. Osegovic, R. S. Drago, *J. Phys. Chem. B* **2000**, *104*, 147–154.

[51] C. Tagusagawa, A. Takagaki, A. Iguchi, K. Takanabe, J. N. Kondo, K. Ebitani, S. Hayashi, T. Tatsumi, K. Domen, *Angew. Chemie Int. Ed.* **2010**, *49*, 1128–1132; *Angew. Chemie* **2010**, *122*, 1146–1150.

[52] V. Gruver, J. J. Fripiat, *J. Phys. Chem.* **1994**, *98*, 8549–8554.

[53] I. B. Sivaev, V. I. Bregadze, *Coord. Chem. Rev.* **2014**, *270–271*, 75–88.

[54] A. Travert, A. Vimont, J.-C. Lavalley, V. Montouillout, M. Rodríguez Delgado, J. J. Cuart Pascual, C. Otero Areán, *J. Phys. Chem. B* **2004**, *108*, 16499–16507.

[55] D. T. Bregante, D. W. Flaherty, *ACS Catal.* **2019**, *9*, 10951–10962.

[56] E. Z. Ayla, D. S. Potts, D. T. Bregante, D. W. Flaherty, *ACS Catal.* **2021**, *11*, 139–154.

10.1002/anie.202100672

WILEY-VCH

RESEARCH ARTICLE

Entry for the Table of Contents

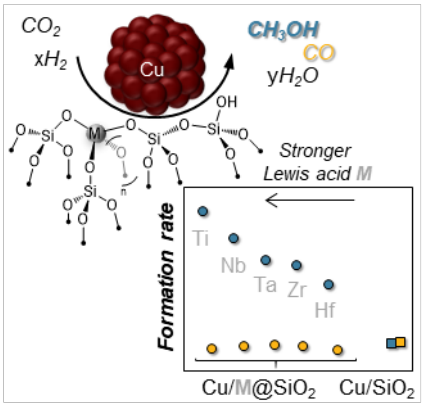

Tailored interfaces. Cu nanoparticles, dispersed on supports decorated with isolated group IV and V metal centers on SiO_2, catalyze the selective hydrogenation of CO_2 to CH_3OH. The promotion of CH_3OH formation rates and selectivity correlates with the Lewis acid strength of the group IV and V dopants, which stabilize surface intermediates at the periphery of Cu nanoparticles.

Institute and/or researcher Twitter usernames: @coperetgroup (CC), @ETH_DCHAB, @Flaherty_Lab (DWF)